

ORIGIN AND FULL CHARACTERIZATION OF THE SECONDARY (ASSEMBLY) HALO BIAS

EDUARD SALVADOR-SOLÉ, ALBERTO MANRIQUE, AND EDUARD AGULLÓ¹

¹*Institut de Ciències del Cosmos. Universitat de Barcelona, E-08028 Barcelona, Spain*

ABSTRACT

The clustering of dark matter halos depends not only on their mass, the so-called primary bias, but also on their internal properties, the so-called secondary bias. While the former effect is well-understood within the Press-Schechter (PS) and excursion set (ES) models of structure formation, the latter is not. In those models, protohalos are fully characterised by their height and scale, which determine the halo mass and collapse time, so there is no room for any other halo property. This is why the secondary bias was believed not to be innate but due to the distinct merger rate of halos lying in different backgrounds, and dubbed assembly bias. However, it is now admitted that mergers leave no imprint in the inner halo properties. In fact, the innate origin of the secondary bias cannot be discarded because, in the more realistic peak model of structure formation, halo seeds are characterized by one additional property: the peak curvature. Here we use the confluent system of peak trajectories (CUSP) formalism to show that peaks lying in different backgrounds have different mean curvatures, which in turn cause them to evolve in halos with different typical inner properties. The dependence we find of the properties on halo background (or halo clustering) reproduces the results of simulations.

Keywords: methods: analytic — cosmology: theory, dark matter — dark matter: halos — galaxies: halos

1. INTRODUCTION

One fundamental property of the Universe is that light does not trace matter. More massive galaxies are more clustered than less massive ones (Capelato et al. 1980) and galaxies of a given mass but different mass-to-light ratios, morphologies or star formation rates are also differently clustered (Faber & Gallagher 1979; Dressler 1980; Poggianti et al. 1999). As the spatial distribution of cosmic objects informs on their formation and evolution, the discovery of those segregations gave rise to a lively “nature vs. nurture” debate (Sanromà & Salvador-Solé 1990; Dressler et al. 1997; Ellis et al. 1997; Smith et al. 2005). In fact, galaxies form and develop within dark matter (DM) halos, which are themselves segregated (biased) in mass as well as in other internal properties, so the spatial distribution of galaxies is tightly coupled to that of halos and their substructure (e.g. Peacock & Smith 2000; Seljak 2000; Zentner et al. 2005; Montero-Dorta et al. 2020; Xu & Zheng 2020).

It is now well-established that the mass segregation of halos (Hauser & Peebles 1973; Bahcall & Soneira 1983), the so-called primary bias, is already imprinted in the primordial density field (Kaiser 1984; Bardeen et al.

1986, hereafter BBKS). However, the reason why halos with the same mass but different internal properties are also differently clustered, the so-called secondary bias, is poorly understood.

The first evidence in simulations of the secondary bias was found by Sheth & Tormen (2004), who noticed that halos in pairs form earlier than more isolated ones. Harker et al. (2006) showed that, in general, the more strongly clustered halos, the smaller their formation time, an effect which was confirmed by other authors (Gao, Springel, & White 2005; Harker et al. 2006; Zhu et al. 2006; Wechsler et al. 2006; Wetzel et al. 2007; Jing, Suto, & Mo 2007). In addition, Wechsler et al. (2006) found that low-mass halos, with the highest concentration, are more clustered, while the opposite is true for high-mass halos. Lastly, Gao & White (2007) showed that the secondary bias affects other internal properties of haloes such as their peak velocity, sub-halo abundance (or halo occupation number) and spin. Those trends were subsequently confirmed and extended to other properties such as the velocity anisotropy and shape (Macciò et al. 2007; Angulo, Baugh, & Lacey 2008; Faltenbacher & White 2010; Lee et al. 2017; Mao, Zentner & Wechsler 2018; Sato-Polito et al. 2019; Chen et al. 2020; Lazeyras et al. 2023; see also Ramakrishnan & Paranjape 2020; Montero-Dorta et al. 2020; Hellwing et al. 2021).

In the PS (Press & Schechter 1974) and excursion set (ES; Bond et al. 1991) models of structure formation, using top-hat and k -sharp smoothing windows, respectively, protohalos are fully characterized by their height and scale, which determine the mass and collapse time of the associated halos regardless of their environment. Thus there is no room in such models for halos of a given mass at a given time to have distinct internal properties according to their background (Gao & White 2007). The fact that the merger history of halos depends on their environment (Gottlöber, Klypin, & Kravtsov 2001; Gottlöber et al. 2002; Fakhouri & Ma 2009, 2010; Wetzel et al. 2007) suggested that the secondary bias was the result of the distinct assembly (merging) history of halos with identical seeds but evolving in different environments. This is why it was dubbed “assembly bias”. However, neither the different merger rate of halos evolving in different environments nor any other evolutionary mechanism explored (Mo et al. 2005; Sandvik et al. 2007; Desjacques 2008; Hahn et al. 2009; Yu et al. 2017) could reproduce the observed properties of the secondary bias.

Furthermore, numerical experiments (Moore et al. 1999; Huss et al. 1999; Hansen et al. 2006; Wang & White 2009; Barber et al. 2012; but see Hester & Tatsiomi 2010; Wang et al. 2020) showed that mergers leave no imprint in halo properties (except in their substructure). The result found by Wang & White (2009) is particularly compelling in the context of the assembly bias: *all internal properties of halos except subhalo abundance are identical in purely accreting halos* (i.e. having undergone monolithic collapse) *than in halos grown hierarchically* (i.e. having suffered major mergers). In addition, Mao, Zentner & Wechsler (2018) and Chen et al. (2020) found that the secondary bias does not correlate with the assembly (or merger) history of halos. Last but not least, Salvador-Solé & Manrique (2021) formally proved such a fundamental characteristic of structure formation.

Zentner (2007) showed that the ES model with a smoothing filter different than the k -sharp one so that protohalos are sensitive to the matter distribution on larger scales leads to halos with formation times dependent on the background. Although, that generic result did not explain the secondary bias found in simulations, it showed that an innate origin of the secondary bias was possible provided the suited model of structure formation. Dalal et al. (2008) noted that, in the peak model where halos form from the collapse of patches around density maxima (peaks) in the smoothed linear Gaussian random density field, protohalos are characterised not only by their height at a given scale, but also by their curvature (i.e. minus the Laplacian of the density field

at the peak scaled to its rms value),¹ which depends on the peak background. Consequently, halos could have different internal properties and formation times arising in a simple natural manner from the specific properties of their seeds, regardless of their assembly history or any other environmental effect.

Unfortunately, some difficulties met in the peak model (see Salvador-Solé & Manrique 2024a, hereafter Paper I) have so far prevented from checking this. If the derivation of the primary bias in the peak model was already challenging, examining whether the secondary bias can be explained in that theoretical framework was even harder: it requires, in addition, connecting the curvature of peaks with the typical internal properties of halos. But that is now feasible thanks to the *ConflUent System of Peak trajectories* (CUSP) formalism, that establishes such a connection from first principles and with no free parameter (Salvador-Solé & Manrique 2021).

In Paper I we applied CUSP to derive in a robust way the primary bias in the peak model. Here we use it to explain and characterize the secondary bias. The layout of the Paper is as follows. In Section 2 we remind the basics of the CUSP formalism. In Section 3, we compare the average density profile of unconstrained halos to that of halos lying in a background. The consequences of this relation on the different internal properties of halos involved in the secondary bias are examined in Section 4. Our results are summarised and the main conclusions are drawn in Section 5.

2. HALO-PEAK CORRESPONDENCE

CUSP allows one to derive all macroscopic halo properties from peak statistics in the linear random Gaussian density field. This is possible thanks to the fact that there is a one-to-one correspondence between halos with M at t (for any particular mass definition) and peaks with density contrast δ in the linear density field at the initial (arbitrary) time t_i , smoothed with a Gaussian filter of scale R . The reader is referred to Salvador-Solé & Manrique (2021) for details. Next we provide a quick overview of this correspondence.

The time t of ellipsoidal collapse of patches around peaks depends not only on their mass and size as in top-hat spherical collapse, but also on their triaxial shape and concentration (Peebles 1969). Nonetheless, the probability distribution functions (PDFs) of ellipticities e , prolatenesses p , and curvatures x of peaks with δ at scale R are very sharply peaked (BBKS), so peaks with any given δ at R have essentially the same fixed values of those quantities, implying that they collapse (and virialize) essentially at the same time t , dependent only on δ at a fixed scale R . Consequently, given any

¹ Peaks also have different ellipticities and prolatenesses, but the typical values of these properties depend on their typical curvature (BBKS).

mass definition of halos fixing their mass M at t , the scale R of the corresponding peaks with $\delta(t)$ at t_i define the relation between R and M , dependent on t in general, for peaks collapsing in halos with M at t .

As shown by [Juan et al. \(2014a\)](#), the relations $\delta(t)$ and $R(M, t)$ can be found, for any given cosmology and halo mass definition, by enforcing the consistency conditions that: (i) at any time t all the DM in the Universe is locked in halos of different masses, and (ii) the mass M of a halo must be equal to the volume-integral of its density profile times the squared radius (see [Sec. 3](#) for derivation of such a density profile). Specifically, if we write those two functions in the form

$$\delta(t, t_i) = r_\delta(t) \delta_c^{\text{th}}(t) \frac{D(t_i)}{D(t)} \quad (1)$$

$$\sigma_0(R, t, t_i) = r_\sigma(M, t) \sigma_0^{\text{th}}(M, t) \frac{D(t_i)}{D(t)}, \quad (2)$$

where $\delta_c^{\text{th}}(t)$ is the linearly extrapolated density contrast for top-hat spherical collapse at t , $a(t)$ is the cosmic scale factor, $D(t)$ is the linear growth factor,² $\sigma_0(R, t, t_i)$ is the Gaussian 0th-order spectral moment at t_i on the scale R corresponding to the mass M at t and $\sigma_0^{\text{th}}(M, t)$ is its top-hat counterpart at t , the functions r_δ and r_σ appear to be well fitted in all cosmologies and halo mass definitions analysed by the analytic expressions

$$r_\delta(t) \approx \frac{a^{dD(t)}(t)}{D(t)} \quad (3)$$

$$D(t) = 1 - d_0 a^{0.435/a(t)}(t)$$

$$r_\sigma(M, t) \approx 1 + r_\delta(t) \mathcal{S}(t) \nu^{\text{th}}(M, t) \quad (4)$$

$$\mathcal{S}(t) = s_0 + s_1 a(t) + \log \left[\frac{a^{s_2}(t)}{1 + a(t)/A} \right],$$

with $\nu^{\text{th}}(M, t) \equiv \delta^{\text{th}}(t, t_i) / \sigma_0^{\text{th}}(M, t_i) = \delta_c^{\text{th}}(t) / \sigma_0^{\text{th}}(M, t)$ equal to the peak height in top-hat spherical collapse. See [Table 2](#) for the values of coefficients d , s_0 , s_1 , s_2 , and A for several cosmologies ([Table 2](#)) and halo mass definitions of interest. Note that while R increases with increasing M , δ decreases with increasing t . We remark that the analytic fitting function $r_\delta(t)$ given by equation (3) only holds up to the present time; its extrapolation to larger times should be taken with caution (see [Sec. 4](#)). When using virial masses, M_{vir} , r_σ is a function of M alone, $r_\sigma(M) = 1 + c / \sigma_0^{\text{th}}(M)$, where $\sigma_0^{\text{th}}(M)$ is the top-hat 0th order spectral moment at the present time and $c = 0.14$ and 0.10 in the *WMAP7* and *Planck14* cosmologies, respectively ([Paper I](#)).

Strictly speaking, some peaks with δ at R are nested into other peaks with the same δ at a larger scale, so

² In the Einstein-de Sitter cosmology, $\delta_c^{\text{th}}(t) = 3(12\pi)^{2/3}/20 = 1.686$ and $D(t) = a(t)$; see e.g. ([Henry 2000](#)) for other cosmologies.

Table 1. Coefficients in the halo-peak relations.

Cosmol.	Mass*	d	$10d_0$	10^2s_0	10^2s_1	10^2s_2	A
WMAP7	M_{vir}	1.06	3.0	4.22	3.75	3.18	25.7
	M_{200}	1.06	3.0	1.48	6.30	1.32	12.4
Planck14	M_{vir}	0.93	0.0	2.26	6.10	1.56	11.7
	M_{200}	0.93	0.0	3.41	6.84	2.39	6.87

* M_{vir} and M_{200} are the masses inside the region with a mean inner density equal to $\Delta_{\text{vir}}(t)$ ([Bryan & Norman 1998](#)) times the mean cosmic density, and 200 times the critical cosmic density, respectively.

Table 2. Cosmological Parameters.

Cosmology	Ω_Λ	Ω_m	h	n_s	σ_8	Ω_b
WMAP7 ^a	0.73	0.27	0.70	0.95	0.81	0.045
Planck14 ^b	0.68	0.32	0.67	0.96	0.83	0.049

^a [Komatsu et al. \(2011\)](#).

^b [Planck Collaboration et al. \(2014\)](#).

they are actually captured by the more massive halo associated with the host peak before achieving full collapse and become subhalos instead of halos at t . Therefore, equations (1) and (2) do not define a *one-to-one* correspondence between halos and peaks. This means that the abundance of peaks with δ and R at t_i must be corrected for nesting in order to obtain the right mass function of halos at t ([Paper I](#)). But in the present [Paper](#) we are not concerned with the peak number density, but with their average curvature, ellipticity, and prolateness, and these properties depend much more strongly on the background density of the peak (i.e. the density contrast at the same point at a larger scale) than on its possible location within another peak (i.e. at a different point with the same δ at a larger scale). Therefore, when calculating these properties, we will ignore the effects of their possible nesting in front of those of their background density.

3. PEAK TRAJECTORY AND HALO DENSITY PROFILE

Given the halo-peak correspondence (eq. [1]-[2]), the equality

$$\frac{\partial \delta(\mathbf{r}, R)}{\partial R} = R \nabla^2 \delta(\mathbf{r}, R) \equiv -x(\mathbf{r}, R) \sigma_2(R) R \quad (5)$$

fulfilled by the density field in *Gaussian smoothing* allows one to identify the peaks (possibly at slightly different points) \mathbf{r} that trace the same evolving halo when the scale and the density contrast are varied accordingly in the (δ, R) plane at t_i ([Manrique & Salvador-Solé 1995](#)).

Specifically, when a halo accretes, the associated peak follows a continuous $\delta(R)$ trajectory, which is only interrupted when the halo undergoes a major merger.³ As shown next, the mean continuous peak trajectory traced by *purely* accreting halos with M_0 at t_0 (t_0 is not necessarily the present time) determines their average density profile. Certainly, halos also suffer major mergers, but, as mentioned in Section 1, the density profile of halos with M_0 at t_0 does not depend on their merging history, so we can assume they evolve by pure accretion in order to derive their average density profile (and any other internal property; see Sec. 4).

3.1. Unconstrained halos

According to equation (5), the *mean* trajectory $\delta(R)$, solution of the differential equation

$$\frac{d\delta}{dR} = -\langle x \rangle [R, \delta(R)] \sigma_2(R) R, \quad (6)$$

with the boundary condition δ_0 at R_0 corresponding to halos with M_0 at t_0 , traces their average mass growth by accretion. In equation (6), $\langle x \rangle (R, \delta)$ is the mean curvature of the peak at the intermediate point δ at R , given by (Manrique & Salvador-Solé 1995)

$$\langle x \rangle (R, \nu) = \frac{G_1(\gamma, \gamma\nu)}{G_0(\gamma, \gamma\nu)}, \quad (7)$$

where G_i is the i th moment of x for the x -PDF (BBKS)

$$G_i(\gamma, \gamma\nu) = \int_0^\infty dx x^i F(x) \frac{e^{-\frac{(x-\gamma\nu)^2}{2(1-\gamma^2)}}}{[2\pi(1-\gamma^2)]^{1/2}} \quad (8)$$

$$F(x) \equiv \frac{(x^3 - x) \left\{ \operatorname{erf} \left[\left(\frac{5}{2} \right)^{\frac{1}{2}} x \right] + \operatorname{erf} \left[\left(\frac{5}{2} \right)^{\frac{1}{2}} \frac{x}{2} \right] \right\}}{2 + \left(\frac{2}{5\pi} \right)^{\frac{1}{2}} \left[\left(\frac{31x^2}{4} + \frac{8}{5} \right) e^{-\frac{5x^2}{8}} + \left(\frac{x^2}{2} - \frac{8}{5} \right) e^{-\frac{5x^2}{2}} \right]}, \quad (9)$$

$x_* \equiv \gamma\nu$ and $\gamma \equiv \sigma_1^2 / (\sigma_0 \sigma_2)$, being σ_j the j -th spectral moment. In the case of power-law power spectra of index n , γ is constant and equal to $[(n+3)/(n+5)]^{1/2}$, while in the case of the Cold Dark Matter (CDM) spectrum, locally close to a power-law with index $n \approx -1.75$ in the range of galactic mass halos, we have $\gamma \approx 0.62$.

Equation (6) shows that the mean curvature of peaks at R determines the accretion rate of the corresponding halos, and that the mean peak trajectory $\delta(R)$ traces the average accretion history of halos with M_0 at t_0 . Moreover, since accreting halos grow inside-out (Salvador-Solé et al. 2012a; Salvador-Solé & Manrique 2021), their accretion history automatically sets their density profile, so the mean peak trajectory $\delta(R)$ determines the average density profile of those halos with M_0 at t_0 .

Specifically, as shown in Salvador-Solé & Manrique (2021), the peak trajectory is the convolution with a Gaussian window of the peak density profile. Thus, one can infer the average density profile of halos with M_0 at t_0 by deconvolving the mean peak trajectory solution of equation (6) and monitoring their monolithic ellipsoidal collapse and virialization (taking into account that both processes preserve the radial mapping of the initial mass distribution; Salvador-Solé et al. 2012a).⁴ The resulting density profile is of the NFW (Navarro, Frenk & White 1995) or the Einasto Einasto (1965) form with a concentration that scales with halo mass as found in simulations over more than 20 orders of magnitude (Salvador-Solé et al. 2023). Moreover, similar procedures using the ellipticity and prolateness of peaks instead of their curvature lead to the average shape and kinematics of halos (see Salvador-Solé et al. 2012b; Salvador-Solé & Manrique 2021).

Interestingly, all these derivations can be applied not only to unconstrained halos (and peaks), but also to halos (peaks) constrained to lie in different backgrounds. Since the curvature, ellipticity, and prolateness of constrained peaks are different from those of unconstrained ones, the properties of halos lying in different backgrounds will also differ from those of unconstrained halos, which could explain the secondary bias. To check this possibility and find the strength of the effect according to the background height, we should compare the different properties obtained for both kinds of objects with varying backgrounds and halo masses. But that would be a very laborious task and would not clarify the physical reason for the results we would obtain. Fortunately, there is an alternative, fully analytic way to do this that only makes use of the change in the mean curvature between unconstrained and constrained peaks.

3.2. Halos Constrained to Lie in a Background

Let us now turn to halos with M_0 at t_0 constrained to lie in a background with matter density contrast $\delta_m(t_0)$. To distinguish the properties of these constrained halos from those of unconstrained ones, we will hereafter denote the former with index “co”. This includes the properties of the corresponding seeds: peaks with density contrast $\delta_0^{\text{co}} = \delta_0$ at R_0 lying in a background with (matter) density contrast $\delta_m(t_i) = \delta_m(t_0)D(t_i)/D(t_0)$ at a scale R_m substantially larger than R_0 .

Even though peaks along a trajectory $\delta^{\text{co}}(R)$ tracing the evolution of accreting halos slightly slosh around a given location when R increases, since the scale of the background at t_i is substantially larger than R , they necessarily keep lying on the same background. As a consequence, the mean trajectory of peaks correspond-

³ Then, a new peak appears with the same δ but a substantially larger scale.

⁴ The same procedure could be applied to individual halos, though the random peak trajectory of a specific halo is unknown, in general.

ing to halos constrained to lie on the background is now the solution of the differential equation

$$\frac{d\delta^{\text{co}}}{dR} = -\langle x \rangle [R, \delta^{\text{co}}(R) | R_m, \delta_m] \sigma_2(R) R, \quad (10)$$

where $\langle x \rangle [R, \delta^{\text{co}}(R) | R_m, \delta_m]$ is the mean curvature of peaks with δ^{co} at R lying in a background with δ_m at scale R_m .

As shown in Manrique & Salvador-Solé (1996), this conditional mean curvature takes exactly the same form as the unconditional one, equation (8), but with $\gamma\nu$ replaced by $\tilde{\gamma}\tilde{\nu}$, given by (BBKS)

$$\tilde{\gamma} = \gamma \left[1 + \epsilon^2 \frac{(1-r_1)^2}{(1-\epsilon^2)} \right]^{1/2} \quad (11)$$

$$\tilde{\nu} = \frac{\gamma(1-r_1)}{\tilde{\gamma}(1-\epsilon^2)} \left[\nu \frac{(1-\epsilon^2 r_1)}{(1-r_1)} - \epsilon \nu_m \right], \quad (12)$$

where $\nu_m \equiv \delta_m / \sigma_{0m}$, being $\sigma_{jm} \equiv \sigma_j(R_m)$,

$$\epsilon \equiv \frac{\sigma_{0h}^2}{\sigma_0 \sigma_{0m}}, \quad r_1 \equiv \frac{\sigma_{1h}^2 \sigma_0^2}{\sigma_{0h}^2 \sigma_1^2},$$

with $\sigma_{jh}(R, R_m)$ defined as σ_j but with R replaced by the squared mean scale $R_h \equiv [(R^2 + R_m^2)/2]^{1/2}$. Note that, in the limit $R_m \rightarrow \infty$, ϵ vanishes, and we have $\tilde{\gamma} = \gamma$ and $\tilde{\nu} = \nu$, so the mean curvature of constrained peaks becomes equal to that of unconstrained ones, as expected.

With those expressions, the quantity $\tilde{\gamma}\tilde{\nu}$ takes the explicit form

$$\tilde{\gamma}\tilde{\nu} = \frac{\delta(\sigma_{0m}^2 \sigma_1^2 - \sigma_{0h}^2 \sigma_{1h}^2) - \delta f_m(\sigma_{0h}^2 \sigma_1^2 - \sigma_{1h}^2 \sigma_0^2)}{\sigma_2(\sigma_0^2 \sigma_{0m}^2 - \sigma_{0h}^4)}. \quad (13)$$

At this point, it is convenient to adopt the same approximation used in Paper I. Taking into account that R_m is substantially larger than R (say, $R_m \gtrsim 3R$), R^2 can be neglected in front of R_m^2 , so expression (13) becomes $\tilde{\gamma}\tilde{\nu} = \gamma\nu_e$, where $\nu_e = \delta_e / \sigma_0$ is defined in terms of the effective density contrast $\delta_e = \delta - q(R_m)\delta_m$, being $q(R_m) \equiv \sigma_0^2(R_m/\sqrt{2})/\sigma_0^2(R_m)$. In the case of power-law power spectra, q is constant and equal to $2^{(n+3)/2}$ while, in the case of the CDM spectrum locally close to a power-law, the same expression approximately holds with the effective value of n corresponding to the scale R_m . From now on, we adopt the effective constant value $q \approx 1.6$ shown in Paper I to yield very good results for galactic halo backgrounds.

Thus, the mean average curvature of peaks with δ^{co} at R lying in a background δ_m , $\langle x \rangle [R, \delta^{\text{co}}(R) | R_m, \delta_m]$, is very nearly equal to the average curvature of unconstrained peaks with effective density contrast $\delta_e^{\text{co}} = \delta^{\text{co}} - q\delta_m$ at R . Consequently, the mean trajectory of

constrained peaks is very nearly given by the solution of the equation

$$\frac{d\delta^{\text{co}}}{dR} = -\langle x \rangle [R, \delta^{\text{co}}(R) - q\delta_m] \sigma_2(R) R, \quad (14)$$

for the boundary condition $\delta_0^{\text{co}} = \delta_0$ (both kinds of peaks collapse at the same time t_0) at R_0 . Since $q\delta_m$ is constant, we can re-write equation (14) as

$$\frac{d\delta_e}{dR} = -\langle x \rangle [R, \delta_e(R)] \sigma_2(R) R, \quad (15)$$

showing that the mean trajectory $\delta^{\text{co}}(R)$ of constrained peaks coincides with the mean trajectory $\delta_e(R)$ of some equivalent unconstrained ones, with boundary condition $\delta_{e0} = \delta_0 - q\delta_m$ at R_0 .

Given the relation between the mean peak trajectory and the average halo density profile, we are led to the conclusion that *the average density profile of halos with M_0 at t_0 lying in a background $\delta_m(t_0)$ is equal to the average density profile of the associated unconstrained halos* (from now on simply the unconstrained halos) *with M_0 at $t_{e0} \equiv t(\delta_0 - q\delta_m)$ ($t_{e0} > t_0$), being $t(\delta)$ the inverse of the function $\delta(t)$ given by equation (1). Note that, according to equation (6), this also means that halos lying in different backgrounds have distinct accretion rates (not to mix up with distinct merger rates), in agreement with the results of simulations (Lee et al. 2017; Chen et al. 2020).*

4. SECONDARY BIAS

In Section 3 we saw that halos with M_0 at t_0 lying in different backgrounds arise from peaks with δ_0 at R_0 having different average curvatures, and hence, tracing different $\delta(R)$ trajectories. In the present Section we will see that, as a consequence, the corresponding haloes have different formation times (z_f), concentrations (c), peak velocities (V_{max}), subhalo abundances (N_s), kinematic profiles (velocity dispersion σ and anisotropy β), triaxial shapes (ellipticity e and prolateness p), and spins (λ) as found in simulations (Sheth & Tormen 2004; Gao, Springel, & White 2005; Harker et al. 2006; Wechsler et al. 2006; Gao & White 2007; Lee et al. 2017; Mao, Zentner & Wechsler 2018; Sato-Polito et al. 2019; Chen et al. 2020).

One indicator, used in the pioneer work by Sheth & Tormen (2004), that a property P is biased is that its median value v^{co}/v in halos with M_0 at t_0 lying in regions with different halo overdensities $\delta_h \approx b\delta_m(t_0)$, where b is the linear halo bias (Paper I), scaled to the median value v in unconstrained halos depends on $\delta_m(t_0)$. To show this in the case of properties directly related to the halo density profile we will use that their median values coincide with the values of those properties in a halo with the average density profile. Indeed, the proof given in (Salvador-Solé et al. 2023) for the concentration automatically translates to any property of that kind,

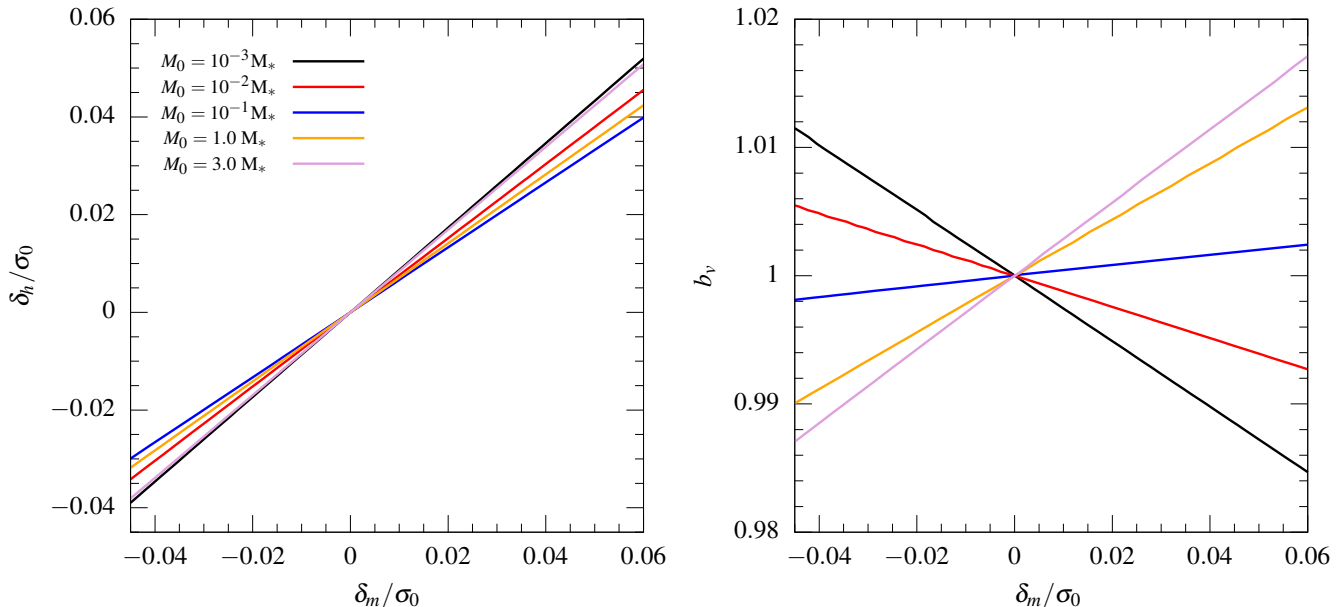


Figure 1. Two different measures of halo clustering: halo overdensity (left panel) and the bias parameter b_v defined in the text (right panel), as a function of the background matter overdensity $\delta_m(t_0)$ (for simplicity, we drop the argument t_0) for several virial masses M_0 in the *Planck14* cosmology at $z_0 = 0.5$.

provided only it is a monotonic function of the concentration. For the remaining properties, namely the halo shape and spin, we will directly use the corresponding median values.

Another indicator of a biased property, introduced by Wechsler et al. (2006) and used in most studies of secondary bias, is that the quantity $b_v \equiv \sqrt{\xi_h(r; v^{\text{co}})/\xi_h(r)}$, where $\xi_h(r; v^{\text{co}})$ and $\xi_h(r)$ are the autocorrelations at the scale M_0 of halos with M_0 and a specific value v^{co} of the property and with M_0 alone, respectively, depends on v^{co} (and differs from unity). As readily seen by replacing $\xi_h(r)$ by $b^2\xi(r)$ in the definition of b_v , this parameter is nothing but b^{co}/b , where b^{co} is the linear bias of halos with M_0 and v^{co} , given by the same expression as the plain linear halo bias b derived in Paper I,⁵ but with $\langle x \rangle(R_0, \delta_0)$ of peaks with δ_0 at R_0 replaced by $\langle x \rangle(R_0, \delta_{e0})$ with $\delta_{e0} = \delta_0 - q\delta_m$.

Since each of these indicators has its own interest (the simplicity of the former case, and the frequent use of the latter), we will analyze both. It is important to realize that the median v^{co}/v vs. δ_h and the b_v vs. v^{co}/v relations result from the parametrization through $\delta_m(t_0)$ of two more fundamental relations: (i) the v^{co}/v vs. $\delta_m(t_0)$ relations, and (ii) the δ_v or δ^{co} vs. $\delta_m(t_0)$ relations. Relations (i) for the different properties P will be derived below, while the two P -independent (see their definition above) relations (ii) are shown in Figure 1.

In this Figure we see that, while δ_h is linear with $\delta_m(t_0)$ with relatively similar positive slopes b for all relevant M_0 , b_v is also linear with $\delta_m(t_0)$ but with a slope that markedly depends on M_0 , with the opposite sign for M_0 lower or higher than a few $10^{-1}M_*$ (slightly less than M_*) for virial masses in the *Planck14* (*WMAP7*) cosmology, where M_* is the cosmology-dependent typical mass of top-hat spherical collapse (solution of the equation $\sigma_0^{\text{th}}(M_*, t_0) = \delta_c^{\text{th}}(t_0)$). The behavior of both relations is well-understood: the larger the background $\delta_m(t_0)$, the higher the overdensity δ_h of halos of mass M_0 lying in it, while the behavior of b_v with δ_m arises from the value of $\langle x \rangle(R, \delta_0 - q\delta_m)$, being $\langle x \rangle(R, \delta)$ a monotonically increasing or decreasing function of δ_m depending on the value of M_0 . This means that the behavior of b_v has nothing to do with the more or less marked clustering of halos with fixed values of any property P when M_0 is varied. It is simply due to the behavior of this clustering indicator with $\delta_m(t_0)$.

Relations (ii) combined with relations (i) derived below, approximately satisfying

$$\frac{v^{\text{co}}}{v} \approx 1 + \left. \frac{d v^{\text{co}}}{d \delta_m} \right|_{\delta_m=0} \delta_m + \frac{1}{2} \left. \frac{d^2 v^{\text{co}}}{d \delta_m^2} \right|_{\delta_m=0} \delta_m^2 \quad (16)$$

in small enough δ_m ranges (see Figure 2), cause the v^{co}/v vs. δ_h and b_v vs. v^{co}/v plots, with the v^{co}/v limits covering the same δ_m range, to be very similar if not identical for all properties P . Thus, we will only show them for two halo properties: the concentration and the formation time. This is enough to illustrate the great similarity in the plots of all properties except for their

⁵ As shown in Paper I, the linear bias b calculated by means of CUSP using Gaussian smoothing coincides with those found in simulations using top-hat smoothing.

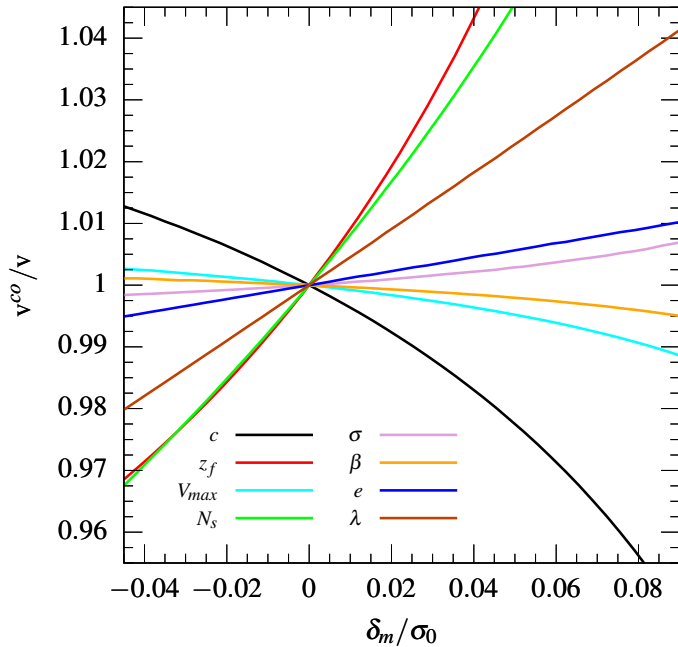


Figure 2. Comparison between the predicted bias in the different properties analyzed here for halos with virial mass $M_0 = M_*$ in the *Planck14* cosmology. (A color version is available in the online journal.)

decreasing or increasing trends with δ_m , and to facilitate the comparison of our predictions to the results of simulations in these best studied cases.

All Figures shown in this Paper are for M_{vir} masses, the *Planck14* cosmology, and redshift $z_0 = 0.5$. The reason for not adopting $z_0 = 0$ is that the collapse time of the equivalent unconstrained peaks, $t_e = t(\delta_0 - q\delta_m)$, exceeds in this case the present time and goes beyond the interval used to fit the function $r_s(t)$ (eq. [1]). Nevertheless, as shown in Paper I, the linear biases b and b^{co} are nearly universal when using M_{vir} masses (and expressing them as functions of ν^{th}), so their ratio b_v is nearly universal too (regardless of how they are expressed). In addition, overdensities are scaled to σ_0 and halo masses to M_* so that all the plots are essentially independent of cosmology (for the suited value of M_*) and redshift. In fact, numerical studies also use snapshots at different cosmic times (up to a redshift as large as $z_0 = 3$) so as to enhance the resolution of simulations (e.g. Wechsler et al. 2006; Gao & White 2007) and scale similarly all quantities with the same purpose.

One final remark is in order. To facilitate obtaining fully analytic expressions for the v^{co}/v vs. $\delta_m(t_0)$ relations we will take advantage that the average density profile of unconstrained halos with M_0 at t_0 is well approximated (Salvador-Solé et al. 2023) by the NFW an-

alytic profile (Navarro, Frenk & White 1995),

$$\rho(r) = \rho_c \frac{4r_c^3}{r(r+r_c)^2}, \quad (17)$$

where r_c and ρ_c are the so-called core radius and characteristic density, respectively. Another useful quantity related to this profile is the mass inside the core radius r_c , $M_c = 16\pi r_c^3 f(1)\rho_c$, where $f(x) = \ln(1+x) - x/(1+x)$, related to the total mass M through

$$M_c = \frac{f(1)}{f(c)} M_0, \quad (18)$$

being c the halo concentration. The price we must pay for this is that, since the fit to the analytic NFW profile is not perfect, the best fitting values of r_c slightly vary with time even though the real core radius is kept unchanged when the density profile grows inside-out (Salvador-Solé, Manrique, & Solanes 2005). Since this spurious effect is more marked for low mass halos, our predictions are only shown for halos with masses $M_0 > 10^{-3} M_*$.

4.1. Concentration

The concentration c of a halo is defined as the total radius over the core radius, $c = r_0/r_c$. Since the virial radius r_0 of all halos with M_0 at t_0 is the same,

$$r_0 = \left[\frac{3M_0}{4\pi\Delta_{\text{vir}}(t_0)\bar{\rho}(t_0)} \right]^{1/3}, \quad (19)$$

the concentration c^{co} of constrained halos with M_0 at t_0 can only differ from the concentration c of unconstrained ones through their distinct core radius.

As shown in Section 3.2, the density contrast of the equivalent unconstrained peaks leading to the average density profile of constrained halos with M_0 at t_0 (or redshift z_0) is $\delta_{e0} = \delta_0 - q\delta_m$, which is smaller than δ_0 . Consequently, the collapse time of the equivalent unconstrained halos, $t_e = t(\delta_0 - q\delta_m)$, is larger than t_0 (and the corresponding redshift $z_e \equiv z(t_e)$ smaller than z_0). As mentioned, CUSP allows one to compute the density profile of unconstrained halos and, from it, their median concentration. Specifically, unconstrained halos with mass M_0 at t_0 (or z_0), with the characteristic mass M_c (eq. [18]) and total radius r_0 (eq. [19]), have a median concentration c satisfying (Salvador-Solé et al. 2023)

$$c = \frac{r_0}{r_{c*}} \left(\frac{M_c}{M_{c*}} \right)^{-\tau(M_c, t_0)}, \quad (20)$$

where

$$\tau(M_c, t_0) = \tau_{c*} \left[1 + t_1 \left(\frac{M_c}{M_{c*}} \right)^{t_2} (1 + z_0)^{t_3} \right], \quad (21)$$

Table 3. Coefficients of the mass-concentration relation for NFW halos.

Cosmology	Mass	r_{c*} (Mpc)	M_{c*} (M_\odot)	τ_{c*}	t_1	t_2	t_3
WMAP7	M_{vir}	9.46×10^{-5}	1.00×10^5	0.325	0.183	.0145	-0.187
	M_{200}	9.75×10^{-5}	1.00×10^5	0.317	0.199	.0134	-0.121
Planck14	M_{vir}	8.04×10^{-5}	1.00×10^5	0.280	0.382	.00854	-0.110
	M_{200}	8.59×10^{-5}	1.00×10^5	0.314	0.219	.0134	-0.131

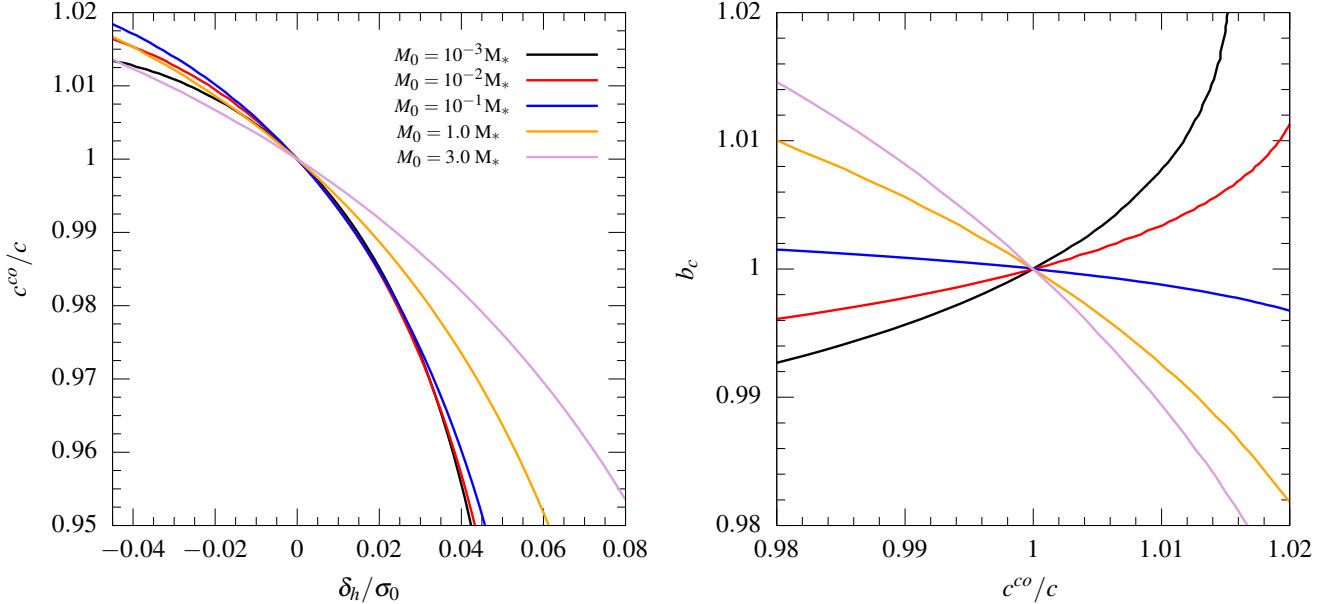


Figure 3. Left panel: Ratio of median concentrations of constrained and unconstrained halos, c^{co}/c , as a function of the halo overdensity δ_h scaled to the rms matter density contrast σ_0 for halos of several virial masses in the *Planck14* cosmology. Right panel: Bias parameter b_c (i.e. b_v for $v = c$) commonly used in numerical studies of the secondary bias as a function of c^{co}/c . (A color version is available in the online journal.)

with coefficients τ_{c*} , r_{c*} , M_{c*} , t_1 , t_2 , and t_3 given in Table 3.⁶

This relation also holds, of course, for the equivalent *unconstrained* halos collapsing at t_e (redshift z_e). Given that the equivalent unconstrained halos grow inside-out, their average density profile at t_0 is also of the NFW form with the same core radius and a smaller concentration c^{co} because the total radius is smaller, $r_0^{\text{co}} < r_e$. Thus, using the redshift dependence of the median concentration of unconstrained halos, $c \propto (1+z)^{-1}$ (Salvador-Solé et al. 2023), we have

$$c^{\text{co}} = c_e \frac{1+z_e}{1+z_0}. \quad (22)$$

⁶ Expressions (20)-(21) coincide with those given in Salvador-Solé et al. (2023), but they are presented in a more compact way, with the coefficients t_i redefined accordingly.

As mentioned, the higher the background density $\delta_m(t_0)$, the lower z_e , so equation (22) tells that the smaller c^{co} compared to c_e . But c^{co} compared to c also depends on M_0 because c_e does. Specifically, taking into account that the unconstrained halos with concentrations c_e and c satisfy equations (20)-(21) for the total radii r_e and r_0 , characteristic masses M_{ce} and M_c , and times t_e and t_0 , respectively, equation (22) leads to

$$\frac{c^{\text{co}}}{c} = \frac{(M_c/M_{c*})^{\tau(M_c, t_0)}}{(M_{ce}/M_{c*})^{\tau(M_{ce}, t_e)}} \left[\frac{\Delta_{\text{vir}}(t_0)}{\Delta_{\text{vir}}(t_e)} \right]^{1/3}. \quad (23)$$

The predicted dependence of the typical concentration c^{co} of halos with M_0 at t_0 lying in an overdensity region δ_h of halos with M_0 is shown in the left panel of Figure 3, while the dependence of b_c (i.e. b_v for $v = c$) for halos with M_0 and c^{co} at t_0 is shown in the right panel. In the latter we see that, as found in simulations, for low-mass halos the higher the concentration, the higher $b_c \equiv b^{\text{co}}/b$, while the opposite is true for high-mass halos

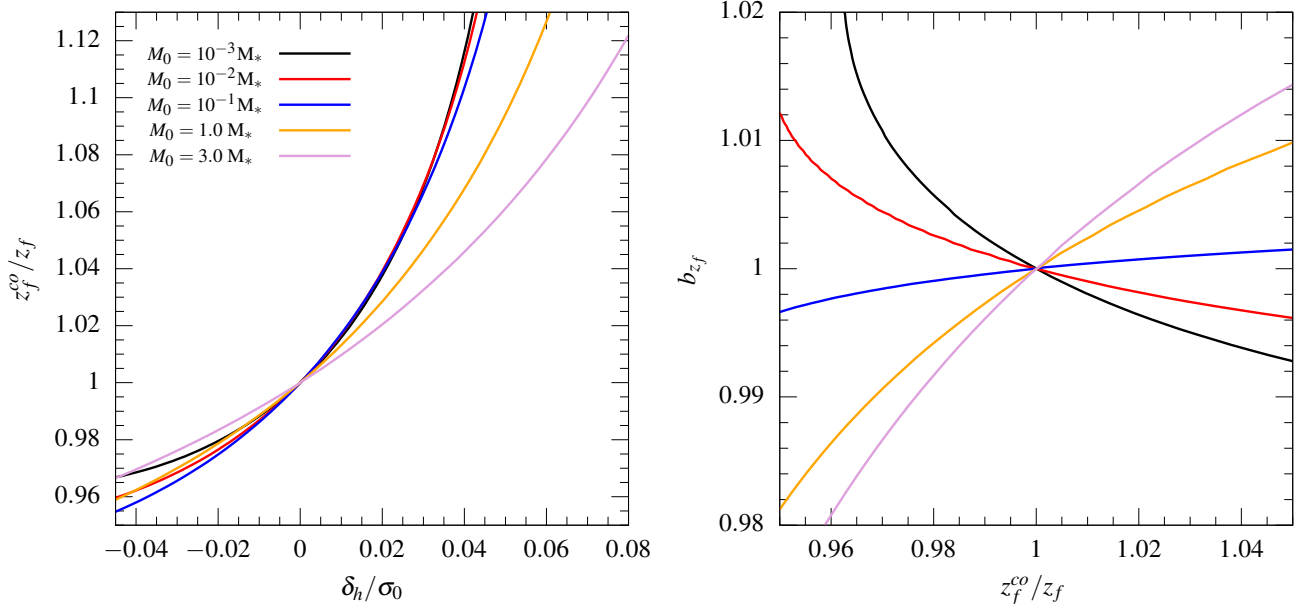


Figure 4. Same as Figure 3 but for the halo formation time. The limits in the abscissa of the left panel correspond to those of in the left panel of that Figure. (A color version is available in the online journal.)

(compare this plot with Fig. 4 of Wechsler et al. 2006). However, as seen in the left panel, the typical value of c^{co}/c is monotonically decreasing with increasing δ_h regardless of the halo mass. This clearly shows that, for the reasons explained at the beginning of this Section, the reversal of the b_c vs. c^{co}/c relation from low to high masses has no physical relevance.

4.2. Formation Time

The formation time t_f (or formation redshift z_f) of a halo with M_0 at t_0 is defined as the time (redshift) at which the halo reached half its current mass. Since the higher the concentration of a halo, the larger its mass fraction at small radii, the earlier they have also formed.

More specifically, the half-mass radius r_h is related to the formation time, t_f of unconstrained halos with M_0 at t_0 through (see eq. [19])

$$r_h = \left[\frac{3M_0/2}{4\pi\Delta_{\text{vir}}(t_f)\bar{\rho}(t_f)} \right]^{1/3}. \quad (24)$$

On the other hand, in NFW halos with mass M_0 , radius r_0 , and concentration c , the mass inside the radius r satisfies the relation

$$M(r) = M_0 \frac{f(cr/r_0)}{f(c)}, \quad (25)$$

implying that the radius r_h encompassing half their total mass is the solution of the implicit equation

$$\frac{f(cr_h/r_0)}{f(c)} = 0.5. \quad (26)$$

Therefore, equation (26) with r_h given by equation (24) is an implicit equation for the formation time t_f of halos with M_0 at t_0 .

The previous relations also hold, of course, for the equivalent unconstrained halos (of the NFW form) with M_0 at t_0 by simply replacing c by c^{co} . Consequently, taking into account that Δ_{vir} and f are very smooth functions of their respective arguments, both implicit equations lead, after some algebra, to the following relation between the typical formation redshift z_f^{co} of constrained and unconstrained halos with M_0 at t_0

$$\frac{z_f^{\text{co}}}{z_f} \approx 1 + \left(\frac{c}{c^{\text{co}}} - 1 \right) \frac{1 + z_f}{z_f}. \quad (27)$$

Since the more strongly clustered halos, the lower their concentration, equation (27) tells that the larger their formation redshift.

As can be seen in Figure 2, the dependence of the formation redshift with $\delta_m(t_0)$ is substantially steeper than that of the concentration, and shows the opposite trend. Yet, the plots in each panel of Figure 4 are identical (very similar in other cases below) to those of Figure 3 except for the opposite trend of the curves. In particular, in the right panel of Figure 4 we see the same reversal of the trend in the b_{z_f} vs. z_f^{co}/z_f relation from low to high masses. We remark that constrained halos with very low masses (say, with $M_0 < 10^{-1}M_*$) will form at such high redshifts that their mass at formation will often fall below the halo mass limit of simulations, so they will not be included in numerical studies of this bias. As a consequence, the reversal of the trend should be more difficult to detect for the formation redshift than for the concentration, which explains the doubts

about that particular feature regarding the formation time found in the literature (e.g. [Jing, Suto, & Mo 2007](#); [Gao & White 2007](#)).

4.3. Peak Velocity

The peak velocity v_p of a halo is the maximum value reached by its circular velocity profile $V(r)$ defined as

$$V(r) = \left[\frac{GM(r)}{r} \right]^{1/2}, \quad (28)$$

where $M(r)$ is the mass inside r and G is the gravitational constant. Obviously, the more concentrated a halo of a given total mass, the steeper the profile $M(r)$, so the higher also the peak velocity. Let us put this in a more quantitative way.

By differentiating equation (28), we have that the radius r_{\max} marking the maximum circular velocity or peak velocity V_{\max} satisfies

$$\frac{V(r_{\max})}{2r_{\max}} \left[\frac{d \ln M}{d \ln r} \Big|_{r_{\max}} - 1 \right] = 0, \quad (29)$$

implying $4\pi r_{\max}^3 \rho(r_{\max}) = M(r_{\max})$, which, in NFW halos with M_0 and r_0 at t_0 , leads to $r_0/(cr_{\max}) = f^{-1/2}(cr_{\max}/r_0) - 1$. Plugging such an expression of r_{\max} into equation (28) and using the NFW expression for $M(r_{\max})/r_{\max}$, we obtain

$$V_{\max} = \left[\frac{GM_0}{r_0} \frac{h(cr_{\max}/r_0)}{h(c)} \right]^{1/2}, \quad (30)$$

where $h(x) = f(x)/x$.

Replacing c by c^{co} , we obtain the homologous expression for halos of the same mass M_0 at the same time t_0 constrained to lie in a background. And, from both relations, we arrive at the following ratio between the peak velocity V_{\max}^{co} in constrained halos and its counterpart V_{\max} in unconstrained ones,

$$\frac{V_{\max}^{\text{co}}}{V_{\max}} = \left[\frac{h(c)}{h(c^{\text{co}})} \right]^{1/2}, \quad (31)$$

where we have used that $h[(cr_{\max})^{\text{co}}/r_0]$ equals $h[(cr_{\max})/r_0]$ as cr_{\max}/r_0 and $(cr_{\max})^{\text{co}}/r_0$ are solutions of the same implicit equation mentioned above.

In Figure 2 we see that the $V_{\max}^{\text{co}}/V_{\max}$ decreases with increasing $\delta_m(t_0)$ like c^{co}/c though substantially less steeply. In this sense, even though the peak velocity is often used to evidence the concentration bias because V_{\max} is simpler to measure than c (e.g. [Gao & White 2007](#); [Angulo, Baugh, & Lacey 2008](#)), one must bear in mind that the former has a much less marked bias than the latter. What is instead a very good indicator of the concentration bias (though with the opposite trend) is the bias in the peak velocity radius since one is then led to $r_{\max}^{\text{co}}/r_{\max} = c/c^{\text{co}}$.

4.4. Subhalo Abundance

The results of Section 3 were obtained assuming purely accreting halos. This was justified because the properties of halos with M_0 at t_0 do not depend on their merger history. But, as mentioned, there is one exception: the properties related to substructure.⁷ In particular, the subhalo abundance down to a fixed scaled subhalo mass, M_s/M_0 , N_s , depends on the time t_m of the last major merger of the halo ([Salvador-Solé et al. 2022](#)). Strictly speaking, t_m is not the same as the halo formation time t_f . But, since halos essentially double their mass in major mergers (e.g. [Raig, González-Casado & Salvador-Solé 2001](#)), we can take the latter as a good proxy for the former.

The dependence on t_f of N_s is quite convoluted: apart from depending on the accretion rate of the host halo ([Salvador-Solé, Manrique & Botella 2022a](#)), it depends on its concentration determining the strength at which accreted subhalos are tidally stripped by the halo potential well ([Salvador-Solé, Manrique & Botella 2022b](#)) and the halo merger history ([Salvador-Solé et al. 2022](#)). However, $\log N_s$ in the 20% of unconstrained halos with M_0 at t_0 having suffered the last merger before $0.28t_0$ is $\approx 3/2$ times that of the 20% of objects having suffered it after $0.76t_0$ ([Salvador-Solé et al. 2022](#)). Thus, adopting the approximation that the merger of the two kinds of halos took place just at the time delimiting their respective intervals, we are led to

$$\log(N_s/N_{s0}) \sim -A \log(t_f/t_0), \quad (32)$$

where N_s and N_{s0} are the subhalo abundances of unconstrained halos with M_0 at t_0 formed at t_f and at whatever time, respectively, and factor A satisfies the equation $\log(3/2) = -A(\log 0.28 - \log 0.76)$ is $A \sim 0.41$.

Relation (32) also holds, of course, for the equivalent unconstrained halos with M_0 at $t_{e0} = t(\delta_0 - \delta_m)$, so, dividing both relations, we are led to

$$\frac{N_s^{\text{co}}}{N_s} \approx \left(\frac{t_f^{\text{co}} t_0}{t_f t_{e0}} \right)^{-0.41} \frac{N_{se}}{N_{s0}}, \quad (33)$$

where N_s and N_{se} are the subhalo abundances (down to the same scaled subhalo mass) of unconstrained halos with M_0 at the times t_0 and t_e , respectively. As shown in [Salvador-Solé et al. \(2022\)](#), the average subhalo abundance scales with the mass M_0 of halos (with their own typical concentration) as $N_s \propto (M_0/10^{12} M_\odot)^{0.08}$, with the same proportionality factor at any time t_0 . Since both kinds of unconstrained halos have identical mass M_0 , the last factor on the right of equation (33) cancels

⁷ The reason for this is that subhalos suffer tidal stripping and dynamical friction, so their related properties do not directly arise from the collapse and virialization processes ([Salvador-Solé, Manrique & Botella 2022a,b](#); [Salvador-Solé et al. 2022](#)).

and we arrive at

$$\frac{N_s^{\text{co}}}{N_s} \approx \left(\frac{t_f t_{e0}}{t_f^{\text{co}} t_0} \right)^{0.41}. \quad (34)$$

Given that the higher $\delta_m(t_0)$, the earlier halos form and the later they collapse, equation (34) tells that the larger their amount of subhalos, in agreement with the results of simulations. Both characteristic times are functions of concentration (Secs. 4.1 and 4.2), so the subhalo abundance in halos with the average density profile coincides with its median value, like in all preceding properties. Figure 4 shows that the bias in the subhalo abundance is very similar to that in the formation redshift.

4.5. Kinematics

The velocity dispersion $\sigma(r)$ and anisotropy $\beta(r)$ profiles of haloes with M_0 at t_0 are related to the curvature, ellipticity, and prolateness of the corresponding peaks in a convoluted non-analytic way that involves, in addition, their triaxial shape (Salvador-Solé et al. 2012b). However, taking into account energy conservation and the gravitational origin of the velocity anisotropy, it was possible to prove the existence of two well-known universal relations found in simulations: one for the velocity dispersion profile (Bertschinger 1985; Tylor & Navarro 2001)

$$\sigma(r) \propto \rho^{1/3}(r) r^{1.875/3}, \quad (35)$$

with universal proportionality factor, and the other for the velocity anisotropy profile $\beta(r)$ (Hansen & Stadel 2006)

$$\beta(r) \approx -0.2 \left(\frac{d \ln \rho}{d \ln r} + 0.8 \right). \quad (36)$$

In other words, both kinematic profiles turn out to be fully determined by the density profile itself. The ultimate reason for this is well understood: as mentioned in Section 2, the typical ellipticity and prolateness profiles of peaks are functions of the peak trajectory, which determines the density profile of the final halo (Salvador-Solé et al. 2012b).

Therefore, since the average density profiles of constrained and unconstrained halos are slightly different, the same is must be true for their average velocity dispersion and anisotropy profiles. Specifically, the higher the background density, the higher the halo concentration, and hence, the steeper their density profile. Consequently, the steeper also the velocity dispersion and anisotropy profiles.

Dividing the relations (35) holding for constrained and unconstrained halos, we are led to

$$\frac{\sigma^{\text{co}}(r)}{\sigma(r)} = \left[\frac{\rho^{\text{co}}(r)}{\rho(r)} \right]^{1/3}. \quad (37)$$

In particular, at the virial radius where $\rho(r_0) = M_0 c^2 / (4\pi r_0^3) / [f(c)(1+c)^2]$ we have

$$\frac{\sigma^{\text{co}}(r_0)}{\sigma(r_0)} = \left[\left(\frac{c^{\text{co}}}{c} \frac{1+c}{1+c^{\text{co}}} \right)^2 \frac{f(c)}{f(c^{\text{co}})} \right]^{1/3}. \quad (38)$$

Since the higher $\delta_m(t_0)$, the higher c^{co} , equation (35) tells that the higher also $\sigma^{\text{co}}(r_0)$, in agreement with simulations.

On the other hand, dividing the relations (36) at the virial radius r_0 for the unconstrained and constrained halos, with concentrations c and c^{co} , respectively, where the logarithmic slope of the density profile of NFW halos with M_0 and r_0 satisfies

$$\frac{d \ln \rho}{d \ln r} = - \left[1 + \frac{2}{1 + r_0/(rc)} \right], \quad (39)$$

we arrive at

$$\frac{\beta^{\text{co}}(r_0)}{\beta(r_0)} \approx \frac{0.1 + 1/[1 + (c^{\text{co}})^{-1}]}{0.1 + 1/(1 + c^{-1})}. \quad (40)$$

Since the higher $\delta_m(t_0)$, the higher c^{co} , equation (40) tells that the smaller $\beta^{\text{co}}(r_0)$.

As can be seen in Figure 2, the biases in the velocity dispersion and anisotropy are the less marked among all the properties analyzed.

4.6. Triaxial Shape

As mentioned, the triaxial shape of halos, characterized by their ellipticity ($e \geq 0$) and prolateness ($|p| \leq e$, with p positive for oblate objects and negative for prolate ones), is related to that of the corresponding peaks through the kinematics of the final objects in a convoluted non-analytic way. However, Salvador-Solé et al. (2012b) showed that, globally, the shape of the isodensity contours in halos and protohalos vary with radius in a similar way. Moreover, since the deeper one goes in a halo, the less marked the influence of the kinematics in its shape, so the closer its ellipticity and prolateness to those of the corresponding protohalo. On the contrary, as one goes outwards, the more spherical haloes compared to their seeds. Thus, we will concentrate on the halo shape at small radii, for which simple analytic relations can be derived.

The probability of a given ellipticity and prolateness of peaks is independent of their height ν and decreases with increasing curvature. In particular, the typical asphericity of peaks with δ_0 at R_0 measured through the ellipticity e diminishes with the average curvature $\langle x \rangle$, according to (BBKS)

$$e \approx \frac{1}{\sqrt{5}} \left[\langle x \rangle^2 (R_0, \delta_0) + 6/5 \right]^{-1/2}. \quad (41)$$

Since constrained peaks with δ_0 at R_0 behave as unconstrained ones with $\delta_{e0} = \delta_0 - q\delta_m$ at R_0 , their median

ellipticity takes the form (41) with the average curvature evaluated at δ_{e0} . Consequently, the ratio of median ellipticities *at small radii* (say, at $r \sim r_c$) of constrained and unconstrained halos with *large* M_0 at t_0 , close to those of their corresponding peaks, is

$$\frac{e^{co}}{e} \approx \left[\frac{\langle x \rangle^2(R_0, \delta_0) + 6/5}{\langle x \rangle^2(R_0, \delta_{e0}) + 6/5} \right]^{1/2}. \quad (42)$$

Since $\langle x \rangle(R, \delta)$ increases with increasing δ at fixed R , equation (42) implies that the larger $\delta_m(t_0)$, the larger the typical ellipticity e^{co} . In lower mass halos, the dependence of e^{co}/e on c^{co}/c is less simple, but the trend is similar.

As shown in Figure 2, the ellipticity bias (at small radii and for large mass halos) is quite weak, which agrees with the results of simulations (Chen et al. 2020). In particular, the reversal of the trend in the shape bias is found in simulations to take place at the same mass marking the frontier between the two similar regimes in the concentration bias (Faltenbacher & White 2010), as predicted here.

The same derivation applied to the halo prolateness p leads to a ratio of prolatenesses p^{co}/p in constrained and unconstrained halos of the same form as e^{co}/e , but with the right hand member of equation (42) to the fourth power. Thus, the prolateness bias is predicted to be much more marked than the ellipticity bias.

4.7. Spin

The spin parameter λ used in most studies of the secondary bias (e.g. Gao & White 2007) is defined as (Bullock et al. 2001)

$$\lambda = \frac{J}{\sqrt{2}M_0r_0V_0}, \quad (43)$$

where J is the modulus (vector norm) of the total angular momentum (AM) \mathbf{J} relative to the center of mass (c.o.m.) of the halo with M_0 , and V_0 is its circular velocity at the radius r_0 . According to the Tidal Torque Theory, in linear and moderately non-linear regime \mathbf{J} is kept with the same direction and J increases with time t as $J(t) = a^2(t)D(t)J^L$, being the i th component of the constant Lagrangian protohalo AM given by

$$J_i^L = \epsilon_{ijk} \mathbf{T}_{jl} \mathbf{I}_{lk} \quad (44)$$

where \mathbf{T} is the Hessian of the potential at the c.o.m. of the protohalo at t_i and \mathbf{I} is its inertia tensor (White 1984). Consequently, the ratio of the median AM of constrained and unconstrained halos with M_0 collapsed at the same time t_0 , J^{co}/J , is simply equal to the ratio of their median Lagrangian AM modulus, $(J^L)^{co}/J^L$.

Using CUSP Salvador-Solé & Manrique (2024b) have recently derived the median Lagrangian protohalo AM for unconstrained halos with *virial* mass M_0 at t_0 in the

peak model. The result is

$$J^L(M_0, t_0) \approx \frac{0.521}{\frac{5}{3}m + 3} G \bar{\rho}_0^{-1/3} s^{\frac{5}{3}m} g M^{5/3} \frac{\delta}{D(t_i)}, \quad (45)$$

where $\bar{\rho}_0$ is the present mean cosmic density, $m = -(n+3)/2$, being $n \approx -1.75$ the effective power index of the CDM spectrum at galactic halo masses,

$$s^{-3} = \frac{2}{3\pi} \left(\frac{n+5}{6} \right)^{3/2} G_0(\gamma, \gamma\nu) e^{-\frac{\nu^2}{2}}, \quad (46)$$

and

$$g = \left[\frac{(\gamma\nu)^{1/3}}{\langle x \rangle^2(R_0, \delta_0) + 6/5} \right]^2. \quad (47)$$

Note that $J^L(M_0, t_0)$ is independent, indeed, of the (arbitrary) initial time t_i because $\delta_0/D(t_i)$ is a function of t_0 alone (see eq. [1]). Therefore, taking into account that V_0 is the same in constrained and unconstrained halos with M_0 and r_0 (eq. [28]), we are led to

$$\frac{\lambda^{co}}{\lambda} = \frac{J^{co}}{J} \approx \left[\frac{\langle x \rangle^2(R_0, \delta_0) + 6/5}{\langle x \rangle^2(R_0, \delta_{e0}) + 6/5} \right]^2. \quad (48)$$

Since the higher δ_m , the smaller $\langle x \rangle(R_0, \delta_{e0})$, and the larger the spin as found in simulations (Gao & White 2007). In Figure 2 we see that the spin is among the properties (together with concentration, formation redshift, and subhalo abundance) that show the most marked bias, in agreement with the results of simulations (Mao, Zentner & Wechsler 2018). In addition, the common origin (directly related to the mean protohalo curvature) of the triaxial shape and spin biases is consistent with their observed correlation (Sato-Polito et al. 2019).

5. SUMMARY AND CONCLUSIONS

Cosmological simulations show that halos with the same mass but different internal properties (concentration, formation time, velocity peak, subhalo abundance, kinematics, triaxial shape, and spin) are differently clustered, what is known as secondary bias.

Using the CUSP formalism relating halos with mass M_0 at the cosmic time t_0 with peaks with density contrast δ_0 at scale R_0 in the Gaussian-smoothed random Gaussian density field at an initial (arbitrary) time t_i , we have examined the appealing idea suggested by Dalal et al. (2008) that the secondary bias could arise from the different typical curvature of peaks lying in different backgrounds have different typical curvatures. To do that, we have taken advantage that mergers can be ignored when dealing with the internal properties of halos, and focused on purely accreting objects.

We have shown that the mean curvature of peaks with given δ_0 and R_0 depends on their background density.

In addition, we have demonstrated that the halo shape and spin directly arise from the curvature of the associated peaks, while all the remaining properties entering secondary bias arise from the curvature of peaks along the continuous $\delta(R)$ trajectory tracing the growth of accreting halos, which determine their density profile (Salvador-Solé & Manrique 2021). Consequently, the halo shape, spin, and any property related to the density profile depend on the peak background, or equivalently, on the halo background. And, given the primary bias relating the local halo and matter densities (Paper I), this causes halos with different values of these properties to be differently clustered.

We have found that the mean curvature of peaks constrained to lie in a background is essentially the same as for unconstrained peaks with a slightly different density contrast. This has allowed us to derive simple analytic expressions for the bias in all those halo properties. The predicted median values of these properties in halos lying in specific background densities, or equivalently, the clustering level of halos with specific values of the properties have been shown to agree with the trends found in simulations.

Interestingly, the only difference between distinct properties is in their specific monotonic relation with

the peak curvature. The peak curvature vs. background density, or equivalently, the clustering level of halos whose peaks have a specific curvature is obviously the same for all properties. Consequently, the reversal of the clustering level of halos as a function of the values of any given property from low to high halo masses found in simulations is a general feature. It is inherent to the dependence of curvature on the density contrast and scale of peaks, which does not depend on the particular property considered. Therefore, contrarily to what is commonly believed, such a reversal does not reflect any change with mass of the clustering trend of halos with different values of the property.

Thus, the main conclusion of this work is that the secondary bias, like the primary one, is innate, and it is well reproduced in the peak model of structure formation.

- 1 This work was funded by the Spanish MCIN/AEI/
- 2 10.13039/501100011033 through grants CEX2019-
- 3 000918-M (Unidad de Excelencia ‘María de Maeztu’,
- 4 ICCUB) and PID2022-140871NB-C22 (co-funded by
- 5 FEDER funds) and by the Catalan DEC through the
- 6 grant 2021SGR00679.

REFERENCES

- Angulo R. E., Baugh C. M., Lacey C. G., 2008, *MNRAS*, 387, 921
- Bahcall N. A., Soneira R. M., 1983, *ApJ*, 270, 20
- Barber, J.A., Zhao, H., Wu, X., & Hansen, S. H. 2012, *MNRAS*, 424, 1737
- Bardeen J. M., Bond J. R., Kaiser N., Szalay A. S., 1986, *ApJ*, 304, 15 (BBKS)
- Bertschinger, E. 1985, *ApJS*, 58, 39
- Bond, J.R., Cole, S., Efstathiou, G., & Kaiser, N. 1991, *ApJ*, 379, 440
- Bryan G.L. & Norman M. L., 1998, *ApJ*, 495, 80
- Bullock J. S., Dekel A., Kolatt T. S., Kravtsov A. V., Klypin A. A., Porciani C., Primack J. R., 2001, *ApJ*, 555, 240
- Capelato H. V., Gerbal D., Salvador-Sole E., Mathez G., Mazure A., Sol H., 1980, *ApJ*, 241, 521
- Chen Y., Mo H. J., Li C., Wang H., Yang X., Zhang Y., Wang K., 2020, *ApJ*, 899, 81
- Dalal N., White M., Bond J. R., Shirokov A., 2008, *ApJ*, 687, 12
- Desjacques V., 2008, *MNRAS*, 388, 638
- Dressler A., 1980, *ApJ*, 236, 351
- Dressler A., Oemler A., Couch W. J., Smail I., Ellis R. S., Barger A., Butcher H., et al., 1997, *ApJ*, 490, 577 (D+97)
- Einasto J. 1965, *Trudy Inst. Astrofiz. Alma-Ata*, 5, 87
- Ellis R. S., Smail I., Dressler A., Couch W. J., Oemler A., Butcher H., Sharples R. M., 1997, *ApJ*, 483, 582
- Faber S. M., Gallagher J. S., 1979, *ARA&A*, 17, 135
- Faltenbacher, A. & White, S. D. M. 2010, *ApJ*, 708, 469
- Fakhouri O., Ma C.-P., 2009, *MNRAS*, 394, 1825
- Fakhouri, O., & Ma, C.-P. 2010, *MNRAS*, 401, 2245
- Gao L., Springel V., White S. D. M., 2005, *MNRAS*, 363, L66
- Gao L., White S. D. M., 2007, *MNRAS*, 377, L5
- Gottlöber S., Klypin A., Kravtsov A. V., 2001, *ApJ*, 546, 223
- Gottlöber S., Kerscher M., Kravtsov A. V., Faltenbacher A., Klypin A., Müller V., 2002, *A&A*, 387, 778
- Hahn O., Porciani C., Dekel A., Carollo C. M., 2009, *MNRAS*, 398, 1742
- Hansen, S. H., Moore, B., Zemp, M., et al. 2006, *JCAP*, 1
- Hansen S. H., Stadel J., 2006, *JCAP*, 2006, 014
- Harker G., Cole S., Helly J., Frenk C., Jenkins A., 2006, *MNRAS*, 367, 1039
- Hauser M. G., Peebles P. J. E., 1973, *ApJ*, 185, 757
- Hellwing W. A., Cautun M., van de Weygaert R., Jones B. T., 2021, *PhRvD*, 103, 063517
- Henry, J. P. 2000, *ApJ*, 534, 565
- Hester J. A., Tasitsiomi A., 2010, *ApJ*, 715, 342
- Huss, A., Jain, B., & Steinmetz, M. 1999, *ApJ*, 517, 64

- Jing Y. P., Suto Y., Mo H. J., 2007, *ApJ*, 657, 664
- Juan E., Salvador-Solé E., Domènech G., Manrique A., 2014, *MNRAS*, 439, 719
- Kaiser N., 1984, *ApJL*, 284, L9
- Komatsu E., Smith K. M., Dunkley J., Bennett C. L., Gold B., Hinshaw G., Jarosik N., et al., 2011, *ApJS*, 192, 18
- Lazeyras, T., Barreira, A., Schmidt, F., et al. 2023, *JCAP*, 2023, 023
- Lee C. T., Primack J. R., Behroozi P., Rodríguez-Puebla A., Hellinger D., Dekel A., 2017, *MNRAS*, 466, 3834
- Macciò, A. V., Dutton, A. A., van den Bosch, F. C., et al. 2007, *MNRAS*, 378, 55
- Mao Y.-Y., Zentner A. R., Wechsler R. H., 2018, *MNRAS*, 474, 5143
- Manrique A. & Salvador-Solé E., 1995, *ApJ*, 453, 6
- Manrique A. & Salvador-Solé E., 1996, *ApJ*, 467, 504
- Manrique A., Raig A., Solanes J. M., González-Casado G., Stein, P., Salvador-Solé E., 1998, *ApJ*, 499, 548
- Mo H. J., Yang X., van den Bosch F. C., Katz N., 2005, *MNRAS*, 363, 1155
- Montero-Dorta A. D., Artale M. C., Abramo L. R., Tucci B., Padilla N., Sato-Polito G., Lacerna I., et al., 2020, *MNRAS*, 496, 1182
- Mo H. J., White S. D. M., 1996, *MNRAS*, 282, 347
- Moore B., Quinn T., Governato F., Stadel J., Lake G., 1999, *MNRAS*, 310, 114
- Navarro J. F., Frenk C. S., White S. D. M., 1995, *ApJ*, 275, 720
- Peacock J. A., Smith R. E., 2000, *MNRAS*, 318, 1144
- Peebles P. J. E., 1969, *ApJ*, 155, 393. doi:10.1086/149876
- Planck Collaboration, Ade, P. A. R., Aghanim, N., et al. 2014, *A&A*, 571, AA16
- Poggianti B. M., Smail I., Dressler A., Couch W. J., Barger A. J., Butcher H., Ellis R. S., et al., 1999, *ApJ*, 518, 576
- Press, W. H., & Schechter, P. 1974, *ApJ*, 187, 425
- Raig A., González-Casado G., Salvador-Solé E., 2001, *MNRAS*, 327, 939
- Ramakrishnan S., Paranjape A., 2020, *MNRAS*, 499, 4418
- Salvador-Solé E., Manrique A., Solanes J. M., 2005, *MNRAS*, 358, 901
- Salvador-Solé, E., Viñas, J., Manrique, A., & Serra, S. 2012a, *MNRAS*, 423, 2190
- Salvador-Solé, E., Serra, S., Manrique, A., & González-Casado, G. 2012b, *MNRAS*, 424, 3129
- Salvador-Solé E., Manrique A., 2021, *ApJ*, 914, 141
- Salvador-Solé E., Manrique A., Botella I., 2022a, *MNRAS*, 509, 5305
- Salvador-Solé E., Manrique A., Botella I., 2022b, *MNRAS*, 509, 5316
- Salvador-Solé E., Manrique A., Canales D., Botella I., 2022, *MNRAS*, 511, 641
- Salvador-Solé E., Manrique A., Canales D., Botella I., 2023, *MNRAS*, 521, 1988
- Salvador-Solé E., Manrique A., 2024, accepted for publication in *ApJ* (Paper I).
- Salvador-Solé E., Manrique A., 2024, submitted to *MNRAS*.
- Sandvik H. B., Möller O., Lee J., White S. D. M., 2007, *MNRAS*, 377, 234
- Sanroma M., Salvador-Solé E., 1990, *ApJ*, 360, 16
- Sato-Polito G., Montero-Dorta A. D., Abramo L. R., Prada F., Klypin A., 2019, *MNRAS*, 487, 1570
- Seljak U., 2000, *MNRAS*, 318, 203
- Sheth R. K., Tormen G., 2004, *MNRAS*, 350, 1385
- Smith G. P., Treu T., Ellis R. S., Moran S. M., Dressler A., 2005, *ApJ*, 620
- Taylor, J. E., & Navarro, J. F. 2001, *ApJ*, 563, 483
- Wang K., Mao Y.-Y., Zentner A. R., Lange J. U., van den Bosch F. C., Wechsler R. H., 2020, *MNRAS*, 498, 4450
- Wang, J., & White, S. D. M. 2009, *MNRAS*, 396, 709
- White, S. D. M. 1984, *ApJ*, 286, 38
- Wechsler R. H., Zentner A. R., Bullock J. S., Kravtsov A. V., Allgood B., 2006, *ApJ*, 652, 71
- Wetzel A. R., Cohn J. D., White M., Holz D. E., Warren M. S., 2007, *ApJ*, 656, 139
- Xu X., Zheng Z., 2020, *MNRAS*, 492, 2739. doi:10.1093/mnras/staa009
- Yu H. R., Emberson J., Inman D. et al., 2017, *Nat Astron* 1, 0143
- Zentner, A. R. 2007, *International Journal of Modern Physics D*, 16, 763
- Zentner, A. R., Berlind, A. A., Bullock, J. S., et al. 2005, *ApJ*, 624, 505. doi:10.1086/428898
- Zhu G., Zheng Z., Lin W. P., Jing Y. P., Kang X., Gao L., 2006, *ApJ*, 639, L5